NIST Special Publication 250
NIST SP 250-101

Ultraviolet to Short-wave Infrared Spectral Reflectance

Heather J. Patrick
Clarence J. Zarobila

This publication is available free of charge from:
https://doi.org/10.6028/NIST.SP.250-101

NIST NATIONAL INSTITUTE OF STANDARDS AND TECHNOLOGY
U.S. DEPARTMENT OF COMMERCE

NIST Special Publication 250
NIST SP 250-101

Ultraviolet to Short-wave Infrared Spectral Reflectance

Heather J. Patrick
Sensor Science Division, Physical Measurement Laboratory
Clarence J. Zarobila
Sensor Science Division, Physical Measurement Laboratory (Retired)

This publication is available free of charge from:
https://doi.org/10.6028/NIST.SP.250-101

October 2024

U.S. Department of Commerce
Gina M. Raimondo, Secretary

National Institute of Standards and Technology
Laurie E. Locascio, NIST Director and Under Secretary of Commerce for Standards and Technology

NIST SP 250-101
October 2024

Publication History
Approved by the NIST Editorial Review Board on 2024-10-02

How to Cite this NIST Technical Series Publication
Patrick, HJ and Zarobila, CJ (2024) Ultraviolet to Short-wave Infrared Spectral Reflectance. (National Institute of Standards and Technology, Gaithersburg, MD), NIST Special Publication 250 (NIST SP250) NIST SP250-101. https://doi.org/10.6028/NIST.SP.250-101

NIST Author ORCID iDs
Heather J. Patrick: 0000-0002-9752-3769
Clarence J. Zarobila: 0000-0003-4547-0754

Contact Information
heather.patrick@nist.gov

Abstract

The National Institute of Standards and Technology performs calibrations of spectral reflectance measurements in the ultraviolet (UV) to short-wave infrared (SWIR) spectral regions using the Robotic Optical Scattering Instrument (ROSI) and its associated Reference Integrating Sphere (RIS). This special publication gives a comprehensive overview of the design, operation, and capabilities of this facility. Measurement methods for spectral reflectance, the elements of the uncertainty budget, and validation of the reflectance scale through comparison with NIST's previous reference instrument, the Spectral Tri-function Automated Reference Reflectometer (STARR), are described. Examples of calibration measurements, including specular reflectance of mirrors, bidirectional reflectance of diffuse reflectors, and directional-hemispherical reflectance, are given. Examples of typical calibration reports are also provided.

Keywords

Bidirectional reflectance distribution function; directional-hemispherical reflectance; optical properties of materials; reflectance; reflectance factor; diffuse reflectance; spectral reflectance; specular reflectance.

Table of Contents

List of Tables

List of Figures

1. Introduction

The National Institute of Standards and Technology (NIST) performs SI-traceable spectral reflectance calibrations of spectrally neutral, non-fluorescent samples at room temperature using the Robotic Optical Scattering Instrument (ROSI) and its associated Reference Integrating Sphere (RIS). Three types of reflectance measurements are performed: specular reflectance, bidirectional reflectance, and directional-hemispherical reflectance. Prior to the establishment of ROSI and the RIS, these measurements were provided by the Spectral Tri-function Automated Reference Reflectometer (STARR) [1]. On STARR, while specular and directional-hemispherical measurements were always provided over the ultraviolet to shortwave infrared (UV-SWIR) from 250 nm to 2500 nm, the instrument's capabilities for bidirectional reflectance at generalized combinations of incident and viewing angles, described by the bidirectional reflectance distribution function (BRDF, f_r) or reflectance factor (RF, R) [2], were initially limited to the 250 nm to 1100 nm spectral range of the silicon photodiode. STARR's bidirectional measurements were also limited to in-plane geometries, where the viewing angle is constrained to lie within the plane formed by the incident angle and the sample normal. Over time, to address the needs of the remote sensing community and other stakeholders, STARR's capabilities for 0/45 bidirectional reflectance factor (incident angle θ_i of 0° and viewing angle θ_r of 45°) were expanded into the SWIR [3], and NIST's scale for bidirectional measurements was validated through a bilateral comparison [4]. Additionally, NIST and other national metrology institutes recognized the growing need for out-of-plane spectral BRDF measurements. Goniometric instruments (sometimes referred to as goniospectrophotometers) were developed based on nested, orthogonally mounted rotation stages [5] and robotic arms [6, 7]. To continue to meet the needs of its stakeholders, NIST began developing the next generation reference instrument for specular and bidirectional reflectance, the Robotic Optical Scattering Instrument (ROSI) [8]. ROSI's robotic goniometer expands upon the previous goniometer's capabilities by enabling out-of-plane measurements, with the combination of a robotic arm sample holder and the rotation of the receiver arm allowing reflectance measurements at nearly any combination of incident and viewing angles. This is particularly important, for example, in applications such as remote sensing, where a diffuse reflector may be used as a reflectance standard with the viewing angle rotated azimuthally out of the plane formed by the incident angle and sample normal [9].

The initial ROSI system was introduced in 2013 with the robot-based goniometer, a supercontinuum-fiber-laser-based tunable light source operating from 450 nm to 2450 nm, and a preliminary uncertainty budget [8]. In the past several years, key refinements that have enabled the transfer of all reflectance calibrations from STARR to ROSI were made [10]. To extend the UV operation of ROSI into the 250 nm to 450 nm range, a high-brightness xenon-laser-driven light source that can be coupled into the monochromator to cover wavelengths that are not supplied by the supercontinuum source was added. More recently, the reference integrating sphere (RIS), which shares a light source with the ROSI goniometer, was commissioned for directional-hemispherical reflectance measurements [11].

ROSI and the RIS are now the national reference instruments for specular, bidirectional, and directional-hemispherical reflectance measurements. Calibrations are offered for specular reflectance, in-plane bidirectional reflectance, and directional-hemispherical reflectance. The ROSI goniometer can also perform research measurements in out-of-plane bidirectional geometries. The uncertainty budget has been thoroughly characterized for specular, bidirectional, and directional-hemispherical measurements. Reflectance measurements on ROSI and RIS have been validated through comparisons with STARR for specular and diffuse calibrations.

This document is intended to provide customers with a detailed overview of the capabilities and procedures used in performing specular and bidirectional reflectance measurements using ROSI and directional-hemispherical measurements with the RIS. Calibrations are offered under the NIST Calibration Services Program Service ID Number 38060S, “Special Tests of Spectral Reflectance”, for customer-provided test items [12]. The service is found in the Materials section in the Optical Radiation category of the NIST Storefront. The measurement service is part of the NIST Quality Management System [13], which is based on the International Organization for Standardization (ISO)17025 standard [14].

The organization of this Special Publication is as follows. Section 1, this Introduction, has presented historical background and the motivation for establishing the instruments. Section 2 briefly describes the scope of measurements and the measurement methods. Section 3 describes the design of ROSI and the RIS and expands on their capabilities. Section 4 describes the operation of the instruments. Section 5 discusses data analysis and the sources of measurement uncertainty and includes example values. Section 6 presents instrument validation measurements. Finally, example calibration reports are presented in Appendix A.

2. Scope of Measurements

ROSI and the RIS perform spectral reflectance measurements of spectrally neutral, non-fluorescent samples at room temperature. This publication describes measurements and traceability of specular reflectance, bidirectional reflectance, and directional-hemispherical reflectance using these instruments. Reflectance can be measured at wavelengths from 250 nm to 2400 nm using a narrow-band tunable source with 14 nm full-width at half-maximum (FWHM) spectral bandwidth. Measurements of specular and bidirectional reflectance can be performed on samples with widths from 25.4 mm (1 in) to 300 mm (12 in) and thicknesses up to 40 mm. Calibrations of specular and bidirectional reflectance are provided for in-plane (meaning the illumination, sample normal, and viewing direction are in the same plane) geometries. Out-of-plane (arbitrary illumination and viewing direction not in the plane of incidence) geometries can be accommodated for research. The fundamental quantity for bidirectional measurements is the BRDF, from which the reflectance factor can be calculated. Measurements of directional-hemispherical reflectance are relative to a calibrated standard and samples must be large enough to cover the 37 mm RIS port diameter. Directional-hemispherical reflectance measurements are performed at 8° incident angle with the specular reflectance component included. A comprehensive description of system measurement capabilities can be found in Section 3.

2.1. Measurement Methods

ROSI and the RIS both employ illumination with a narrowband, tunable light source, and broadband detectors for light collection.

Measurements of specular reflectance and bidirectional reflectance are made on the ROSI robotic goniometer using an absolute ratiometric method. The reflectance is determined relative to the flux in the incident beam, without need for a reference sample. For any measurement, there are two positions for the detector: incident and sample. In the incident position, the sample is translated out of the beam, and the detector is rotated to collect the entire radiant flux of the illumination beam. In the sample position, the sample is translated into the beam and rotated to the designated illumination angle, and the detector is rotated to collect the reflected radiant flux at the designated viewing angle. Signals from the incident and sample positions, S_i and S_r, are proportional to the incident and reflected radiant fluxes, respectively.

For specular measurements, the sample reflectance is simply the ratio of S_r to S_i. For diffuse reflectance, the fundamental measurement is the BRDF, f_r. The formal definition of the BRDF is the reflected radiance normalized by the incident irradiance for a uniform sample, that is uniformly illuminated. Two principal measurement methods exist for BRDF: the over-illumination method, in which the whole sample is illuminated with uniform irradiance and the scattered radiance is measured, and the under-illumination method, in which a relatively small spot on the sample is illuminated and a receiver collects all the light scattered into a known solid angle. While there are advantages to both methods, ROSI employs the under-illumination method because it enables the instrument to be used for both specular and diffuse measurements and because it is relatively efficient in its use of light. [15]. In the under-illumination method, the BRDF is calculated from the ratio of S_r to S_i along with the solid angle

over which the reflected light is collected. Sections 2.2.1 and 2.2.2 illustrate the geometries used in specular and diffuse reflectance measurements.

Directional-hemispherical reflectance measurements are made using the RIS. In the RIS, measurements are made relative to a standard using a substitution method. First, the incident beam strikes a calibrated standard placed at one port of the sphere. After measuring the signal arising from the standard, it is replaced with the test sample. From the ratio of the signals from the standard and the sample, and from the calibrated values of the standard, the directional-hemispherical reflectance is calculated. Section 2.2.3 illustrates the geometry for the directional-hemispherical measurements.

Details of the system components, including the tunable light source, robot goniometer, and receiver with broadband detectors, are given in Section 3. The measurement equations for the three measurement types are given in Sections 5.1.1 through 5.1.3.

2.2. Measurement Geometries

2.2.1. In-plane Bidirectional

Measurements where the incident angle θ_{i}, the viewing angle θ_{r}, and the normal to the sample are all in the same plane are described by the in-plane geometry shown in Fig.1. Measurements

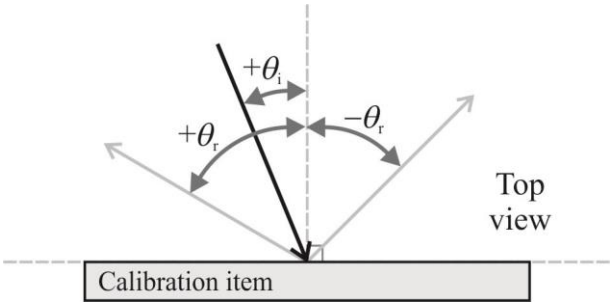

Fig. 1. Top view of illumination and viewing angles θ_{i} and θ_{r}, respectively, for an in-plane geometry reflectance measurement. The "+" and "-" signs in the figure indicate where θ takes on positive or negative values with respect to the top and normal of the calibration item. The top of the calibration item is specified by a fiducial or by other means to fully specify the measurement geometry.

are designated as $\theta_{\mathrm{i}}/\theta_{\mathrm{r}}$, where both θ_{i} and θ_{r} are expressed in degrees. Bidirectional reflectance measurements for diffuse samples can be made at nearly any combination of θ_{i} and θ_{r} within the restrictions given in Section 3.3. Specular reflectance measurements are always in-plane bidirectional, with θ_{i} and θ_{r} equal in magnitude and on opposite sides of the sample normal, for example, 6/-6.

2.2.2. Generalized Bidirectional

The in-plane geometry of Fig. 1 is the most common geometry and is used for all calibration measurements at the time of publication. However, research measurements of bidirectional

reflectance can also be made in the generalized out-of-plane geometry shown in Fig. 2 with the conventions for θ_i, ϕ_i, θ_r and ϕ_r. The incident beam illuminates a small spot on the sample at a selectable polar angle of incidence, θ_i, and azimuthal angle, ϕ_i, and a receiver collects the reflected flux within a solid angle Ω at polar and azimuthal scattering angles θ_r and ϕ_r. When both ϕ_i and ϕ_r are 0° or 180°, the geometry of Fig. 2 reduces to the in-plane case shown in Fig.1, taking the convention that θ_j is positive (negative) when ϕ_j is 0° (180°) for *j* = i or r.

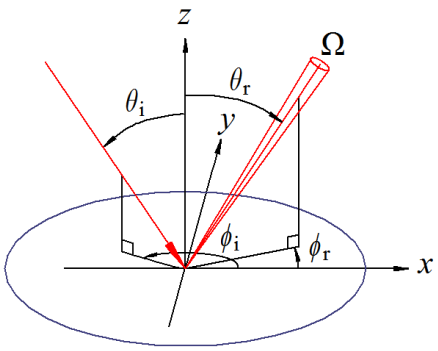

Fig. 2. An illustration of the angles used to describe generalized out-of-plane measurement geometries, where the directions of illumination and viewing are specified with azimuthal and polar angles relative to the sample surface normal.

2.2.3. Directional-hemispherical

The third geometry, employed when making measurements with the RIS, is directional-hemispherical. Light is incident from a specific illumination direction and reflected light is collected from the full hemisphere above the sample. Measurements in this geometry are designated by the incident angle θ_i in degrees, the letter "d" denoting diffuse reflectance, and either "i" or "e" depending on whether light from the specular direction is included or excluded. Measurements with the RIS are made in the 8/di configuration. The geometry for the 8/di configuration is shown in Fig. 3, where the incident light angle has been exaggerated.

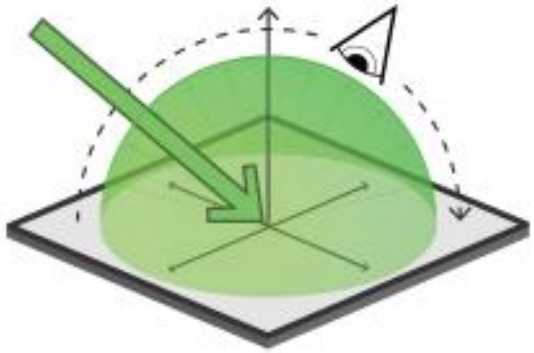

Fig. 3. An illustration of directional-hemispherical measurement

3. The NIST Measurement System

3.1. Overview

Figure 4 shows a schematic of ROSI and the RIS. The system can be functionally divided into three parts, the tunable light source, the robotic goniometer, and the RIS. In the following subsections, each part is described.

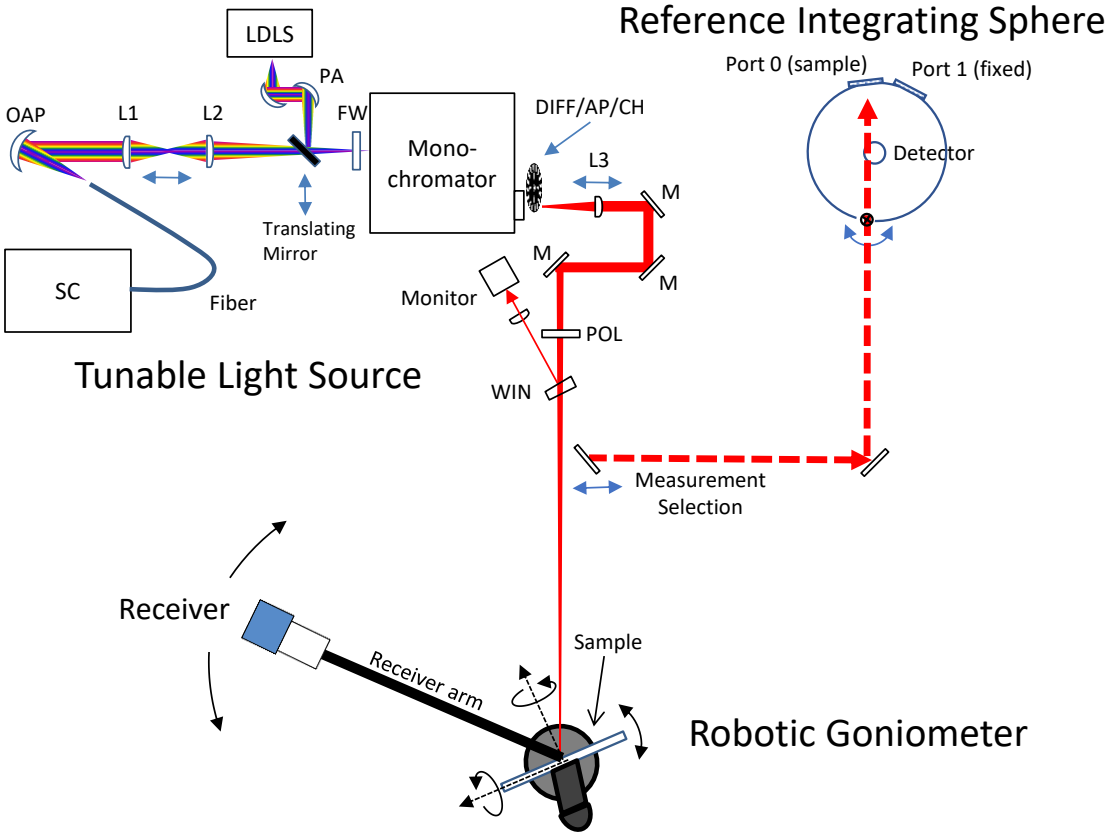

Fig. 4. Schematic of the ROSI instrument and reference integrating sphere. Acronyms are defined in the text.

3.2. Tunable Light Source

The ROSI light source is designed to provide tunable, quasi-monochromatic illumination to the sample with well-defined collimation. The source is based upon two broadband light sources: a supercontinuum fiber laser source (SC), NKT Model N94-170-02,[1] with broadband output from 450

[1] Certain commercial equipment, instruments, or materials are identified in this paper in order to specify the experimental procedure adequately. Such identification is not intended to imply recommendation or

nm to 2400 nm, and a high-brightness laser-driven Xenon light source (LDLS), Energetiq Model EQ-99-PLUS-NA, with output from roughly 220 nm into the short-wave infrared. The source is selected via a translating mirror. For the SC, an off-axis parabola (OAP) collimates the fiber output and is followed by two translatable lenses L1 and L2. These two lenses move according to the selected wavelength to account for chromatic dispersion in the optics and the supercontinuum fiber to ensure high throughput coupling into the monochromator [16]. For the LDLS, a periscope assembly (PA) consisting of a pair of reflective off-axis parabolas are used to match the f-number of the source to that of the monochromator. The single-grating monochromator (Newport Model MS257) includes an order-sorting filter wheel (FW), toroidal optics, and a 4-grating turret with different gratings optimized for different parts of the wavelength range. At the monochromator output, a fused-silica diffuser (DIFF) precedes a 500 µm diameter round aperture (AP). The diffuser helps to expand the focused spot to fill the aperture. The output from the aperture is quasi-monochromatic light tunable from 250 nm to 2400 nm. Typically, the LDLS is used for wavelengths from 250 nm to 500 nm, and the SC is used above 500 nm up to 2400 nm. The optical power reaching the sample is typically 10 to 50 microwatts when using the LDLS, and 100 to 500 microwatts with the SC source. The spectral characteristics of the light source are characterized by direct measurement using the receiver of the robotic goniometer, which includes a small integrating sphere (see Section 3.3). A fiber-coupled spectrometer is connected to the integrating sphere to measure the wavelength and bandwidth of the source. By tuning the source to a range of output wavelengths and observing the difference in commanded wavelength and output wavelength, we determined that the standard uncertainty in wavelength is 0.7 nm, and that the full-width at half-maximum bandwidth of the light source is 14 nm independent of wavelength. The wavelength accuracy of the fiber-coupled spectrometer itself was calibrated using a tunable laser whose wavelength was traceable to a wavemeter.

After the monochromator, a custom, diffraction-limited aspheric lens (L3) images the aperture (AP) to either the center of the goniometer, or the RIS, depending on the position of the selection mirror. The imaging lens produces an approximately top-hat incident beam profile with a 10 mm diameter circular cross section at the sample position. The incident beam is quasi-collimated, with a half angle from the edge of the exit pupil of L3 to the goniometer center equal to 0.37°. Mirrors (M) enable alignment of the source to the goniometer or sphere, and automated translation of L3 ensures that the focus remains at the center of the goniometer or the RIS over the broad wavelength range of the source. A chopper (CH) operating at 75 Hz allows lock-in amplifier detection [17] of received light during measurements. The lock-in amplifier provides the ability to extract weak signals, e.g., those expected when measuring diffuse reflectance. The polarization of the incident light is controlled using a wire-grid linear polarizer (POL) such that linearly polarized light with a selectable rotation angle is delivered to the sample. Finally, a pick-off window (WIN) reflects a small portion of the source output (8 % nominal) and directs it to a power monitor that consists of a lens, a small integrating sphere, and silicon and extended InGaAs (EIGA) detectors attached to the sphere. Use of the monitor provides a means to compensate for any fluctuations in the source power during measurements.

endorsement by the National Institute of Standards and Technology, nor is it intended to imply that the materials or equipment identified are necessarily the best available for the purpose.

3.3. Robot Goniometer and Receiver

Figure 5 shows a photo of the robot and receiver arm that are represented schematically in Fig. 4. An industrial 6-axis robotic arm (Staubli TX60) holds the sample and provides rotation and translation of the sample. The receiver is mounted on an arm connected to a rotation stage that moves the receiver about a vertical axis around the central sample position. The robot is programmed such that the area of interest on the sample face is held at the goniometer center,

Fig. 5. The robot and receiver arm, shown positioned for an out-of-plane scattering measurement of a white diffuse sample.

which is defined by the intersection of the incident light beam and the robot waist rotation axis. The robot and detector arm rotation stage are aligned such that the axis of rotation of the receiver arm is aligned with the robot waist axis. In this way, a constant distance is maintained between the center of the illuminated area of the sample and the center of the precision aperture of the receiver.

Samples are mechanically attached to the sample holder or held using an integrated vacuum chuck. This allows most samples to be held by the edges or the back face, so that the receiver view of the front of the sample is as unobstructed as possible. The thickness of the sample is input to the robot software to bring the sample face to the goniometer center. Samples with lateral dimensions up to 300 mm and thicknesses up to 40 mm can be accommodated. Wedged samples can also be accommodated in software, provided the direction of the wedge is known. Samples which cannot be mounted by the back face can be provided with an adapter that then mounts to the sample holder.

The ROSI receiver consists of a precision aperture followed by a commercially available plano-convex CaF_2 lens and a detector. Two different detectors are used: a 10-mm diameter ultraviolet-enhanced silicon photodiode and an EIGA photodiode mounted on a small integrating sphere that has a 10-mm input port. A translator allows either the surface of the

silicon photodiode or the input port of the sphere to be positioned behind the precision aperture and lens assembly at the detector plane located about 90 mm behind the lens. In the original receiver design, [8] both photodiodes were mounted on the integrating sphere, but after expanding the system to UV wavelengths using the LDLS, the combination of lower spectral power density from the LDLS compared to the SC source and lower sphere throughput at UV wavelengths necessitated a switch to direct illumination for the silicon photodiode.

As introduced in Section 2.1, ROSI performs absolute measurements of BRDF and specular reflectance, meaning that the receiver measures both the incident (S_i) and reflected (S_r) signals. To measure the incident power, the robot moves the sample clear of the incident beam, the receiver faces the incident beam, and the lens focuses the incident beam to the detector. The size of the incident beam underfills the precision aperture, allowing all the incident flux to be collected. When measuring the reflected signal from a specular sample, the reflected beam similarly underfills the precision aperture and detector, ensuring collection of all reflected flux. When measuring reflected signal from a diffuse sample for a BRDF measurement, the solid angle Ω collected by the receiver and the imaging of the sample by the receiver lens must be considered. The precision aperture, along with the distance from sample to aperture, determine the collected solid angle as will be discussed further in Section 5.2.2. The receiver imaging determines the field of view at the sample from which the reflected light is collected. The lens images a 60 mm diameter field of view at the sample to a 10 mm diameter image at the detector plane, which enables the entire illuminated area on the sample, which spreads to an ellipse for non-zero θ_i, to underfill the silicon photodiode or the integrating sphere port and allow collection of all reflected flux within the solid angle for θ_i up to 80°. While the focus

Table 1. Typical source and detector combinations for measurements.

Wavelength Range	Source	Detector
250 nm to 500 nm	LDLS	Silicon photodiode
> 500 nm to 1050 nm	SC	Silicon photodiode
> 1050 nm to 2400 nm	SC	EIGA photodiode on integrating sphere

quality of the image varies with wavelength due to chromatic dispersion, the image quality has been determined through optical modeling to be sufficient for the measurements.

Table 1 shows the typical combinations of light source and detector used as a function of operating wavelength. The silicon photodiode is generally used for measurements between 250 nm to 1050 nm, while the EIGA detector is used from 1050 nm to 2400 nm. Note that each source and detector combination can be operated over some range outside of the nominal wavelengths given in the table. This flexibility allows operating wavelengths to be adjusted for convenience and to check consistency between measurements with different source and detector combinations.

Both the silicon and EIGA photodiodes are amplified using preamps with multiple, adjustable gain settings. The 75 Hz AC-modulated signals are collected using lock-in amplifiers. The lock-in measures only signals in a narrow band around the chopping frequency, and at the correct phase relative to the chopper. The use of lock-in detection minimizes the sensitivity to background light in the room and vastly improves the signal-to-noise ratio compared to unmodulated detection methods. The light source, robotic goniometer, and signal collection

Table 2. Robotic goniometer specifications.

Goniometer Specifications		
Parameter	**Specification**	**Notes**
Robot Type	Articulated Arm	± 0.02 mm positioning repeatability
Number of Axes	6	Enables full hemispherical scanning
Sample size	25 mm (min) to 300 mm (max)	Thickness 0 mm to 40 mm
Sample Payload	3.5 kg nominal; 9 kg max	Including sample holder
Sample Attachment	Mechanical or vacuum chuck	
Sample Translation	± 75 mm from center	Nominal
Receiver Arm Rotation	360° about robot	
Receiver Distance	658 mm	Nominal (measured in practice, see Section 5.2.2)
Optical Specifications (see also Section 3.2)		
Parameter	**Specification**	**Notes**
Measurement Types	Reflectance, BRDF, Reflectance Factor	Bidirectional transmittance distribution function (BTDF) at limited geometries
Measurement Technique	Absolute	
Source type	SC or LDLS	Selectable source input to monochromator
Monochromator	Single-grating Czerny-Turner	Selectable grating via 4-grating turret
Wavelengths	250 nm to 2400 nm	Quasi-monochromatic
Source bandwidth	14 nm	Full-width at half maximum (FWHM) bandwidth
Source wavelength accuracy	0.7 nm	
Incident Beam Diameter	10 mm	At normal incidence
Polarization	Linear incident	Rotatable
Detector types	Silicon, EIGA on integrating sphere	
Solid Angle of Collection	0.0026 sr	Nominal, subtends about 3.3°
Incident angle	θ_i = 0° to 80°, ϕ_i =0° to 360°	Based on 10 mm incident beam
Viewing angle	θ_r= 0° to 88°, ϕ_r =0° to 360°	Full hemispherical scanning, unobstructed view of sample, retroreflection excluded.

are fully automated in software. Table 2 lists additional sample and measurement parameters.

3.4. Reference Integrating Sphere

The RIS is made of a 10 mm thick shell of sintered PTFE and has a 37 mm diameter input port, a 31 mm diameter top detector port, and two 37 mm diameter sample ports labeled Port 0 and Port 1. Figure 6 shows a photograph of the sphere and a top-down schematic with the detector and port configuration. In the photo, Port 1 is the port in the foreground. The PTFE of the sample ports is thinned to a near-knife edge to minimize port edge effects. The rotation stages allow independent rotation about the input port (lower stage, LRS) and the sphere axis (upper stage, URS). For most operations only the lower stage is used, and this stage rotation selects direct illumination of either Port 0 or Port 1. The arrangement of the sample ports and the sphere baffles is currently used for reflectance measurements relative to a standard.

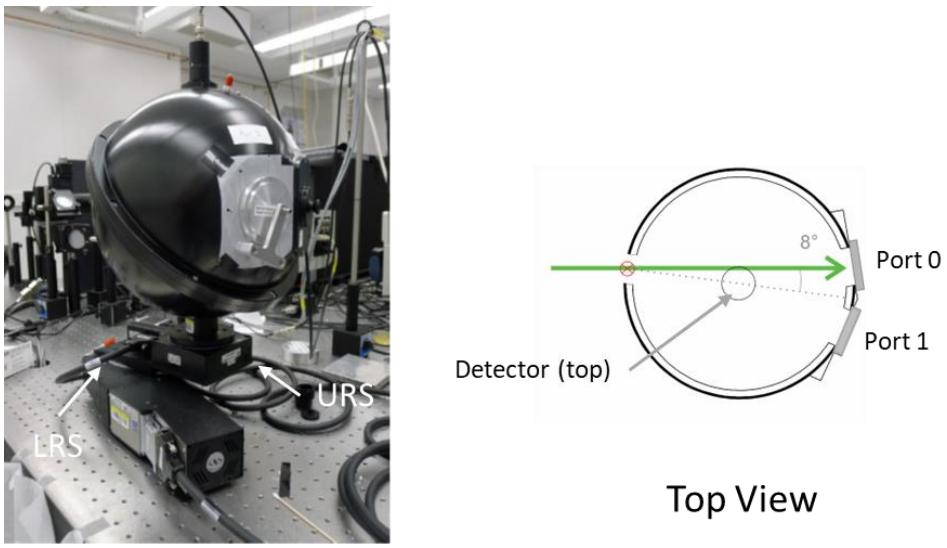

Fig. 6. The Reference Integrating Sphere (RIS)

Figure 7 shows a side view of the sphere. Depending on the wavelength range, either a silicon or EIGA detector is mounted to the sphere using a field-limiting Gershun tube. Upper and lower baffles ensure that light from the first reflection from the sample does not enter the detector field of view. A small baffle between sample ports (not shown) limits first reflections between the sample ports.

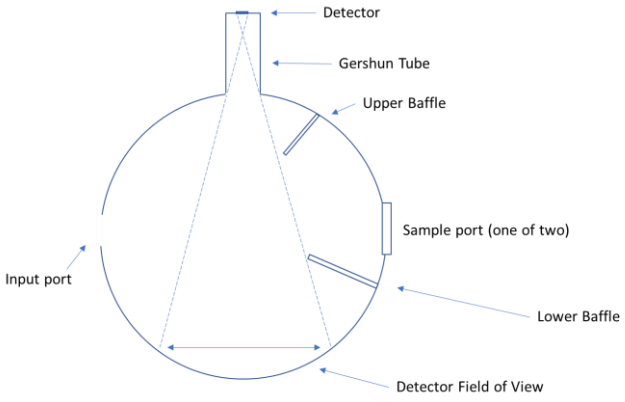

Fig. 7. Side view (not to scale) of the RIS showing upper and lower baffles and detector mounted on a Gershun tube to limit the detector field of view to exclude the lower baffle.

4. Operating Procedures

4.1. Sample Check-in and Handling

Typical samples suitable for a calibration measurement include mirrors in the case of specular reflectance, and diffuse reflectors such as sintered PTFE and ceramics for bidirectional reflectance and directional-hemispherical reflectance. Samples should be spectrally neutral over the requested wavelength range and non-fluorescent. Diffuse samples may have a matte or glossy finish; however, glossy samples are measured only at non-specular geometries, i.e., the instrument is not designed as a glossmeter. Prior to submitting an item for calibration, the customer should consult with measurement staff to determine its suitability. It is strongly recommended that supplied samples include an etched or otherwise permanently affixed serial number and a fiducial mark to identify the top of the sample.

Upon receipt of a calibration item, the item is examined and photographed. Peculiar characteristics such as scars, blemishes and/or scratches are noted. Items found acceptable for calibration are stored in a dedicated area of the calibration laboratory. Samples are handled with gloves. Samples are never cleaned with the exception that dust is removed with a puff of air from an air bulb if necessary.

4.2. Bidirectional Measurements

Before mounting on the robot goniometer, the sample must be measured for thickness and wedge. For flat samples such as mirrors, the thickness is measured using calipers. For diffuse samples, the sample height is measured at its top, left, right and bottom edges using a stylus dial indicator with lens tissue placed between the stylus and sample for protection. If any spacers are required for mounting the sample on the ROSI sample holder, the spacers are included when making the thickness and wedge measurement. Uncertainty in the sample thickness and wedge are estimated using the reproducibility in the edge measurements and the accuracy of the measurement tool for inclusion in the uncertainty budget (see Section 5.2.3). The sample is mounted on the sample holder of the robot goniometer with appropriate offsets input to the goniometer software to align the front surface of the sample with the axis of rotation of the goniometer. For mirrors, in addition to inputting the thickness into the robot software, the reflected beam is checked for its centering on the receiver aperture at the desired specular angle pair.

Prior to measurement, a run definition, which is a series of entries in a database table prescribing the measurement geometries, wavelengths, and polarizations to be performed on a sample, is generated. This information is determined from the requirements specified by the customer. All calibration measurements are made using an in-plane geometry with angles defined as shown in Fig. 1. For research measurements the out-of-plane geometry of Fig. 2 can also be used. The run definition specifies the measurements to be made and the ROSI program automatically calculates the corresponding incident flux measurements that are needed. For example, a run definition that gives a single wavelength and polarization, but multiple viewing geometries, requires only one incident flux measurement.

The sequence of incident flux and reflected radiant flux measurements at the desired geometries, wavelengths and polarizations are controlled by the run definition. In general, there are two positions for the beam in the sample goniometer: incident and sample. In the incident position, the sample is translated out of the beam, and the detector is positioned to collect the incident flux signal, S_{i}. In the sample position, the sample is translated into the beam and rotated to the designated illumination angle, and the detector is rotated to collect the reflected radiant flux signal at the designated viewing angle, S_{r}. S_{i} and S_{r} are proportional to the incident and reflected radiant fluxes, respectively.

A bidirectional measurement is complete when the run definition is satisfied. The process data function in the ROSI program is used to extract the ratio of S_{r} to S_{i} for each wavelength, polarization, and geometry. The specular reflectance, BRDF, or reflectance factor is calculated as described in Section 5.1.1 and 5.1.2 below.

4.3. Directional-hemispherical Measurements

Directional-hemispherical measurements are performed in the 8/di geometry with the incident light directed to the RIS instead of the goniometer. As shown in Fig. 4, a mirror is introduced into the illumination path immediately after the monitor beam splitter. This mirror directs the illuminating beam to a second mirror which sends the beam to the input port of the RIS.

Prior to measurement using the RIS, a pressed powder PTFE standard is prepared. NIST Technical Note 1413 [18] describes the method for generating a pressed PTFE standard using a tool that consists of a cylindrical volume and an acrylic plunger whose contact surface has been appropriately roughened to provide a matte finish to the pressed puck. Powdered PTFE is introduced into the volume, and the weight of powder carefully measured. After pressing, the resulting thickness of the pressed powder must be at least 10 mm, and the resulting density is 1 g cm^{-3} which is the density necessary to produce the traceable reflectance values. Weidner and Hsia [19] gives values for the 6/di directional-hemispherical reflectance for pressed PTFE for wavelengths spanning 200 nm to 2500 nm. Additional measurements presented in Weidner and Hsia show that the difference between 6/di and 8/di directional-hemispherical reflectance is negligible, allowing the 6/di reference values to be applied to 8/di measurements.

Measurement of the sample reflectance is made by the substitution method, where either the PTFE reference standard or the sample under test is mounted on Port 0. A fixed PTFE target is left in place on Port 1 throughout the measurement. The measurement sequence is shown in Fig. 8. In step 1, the incident beam first illuminates the standard on Port 0, and the reflected radiant flux undergoes multiple reflections within the RIS. A portion of these reflections is viewed by the silicon or EIGA detector (see Fig. 7), producing a signal S_{ss} proportional to the reflectance factor of the standard. The sphere is then rotated about its input port to illuminate the fixed target on Port 1, and the signal S_{fs} is collected. In step 2, the sample under test is substituted for the pressed PTFE standard, and detector signals S_{xx} and S_{fx} are collected. The fixed target measurements are used to correct for the change in sphere efficiency (throughput to the detector) when sample and standard have different reflectance. The sequence is repeated for each wavelength for both horizontal and vertical polarizations, and the reflectance of the sample is calculated from the detector signals as discussed in Section 5.1.3 below.

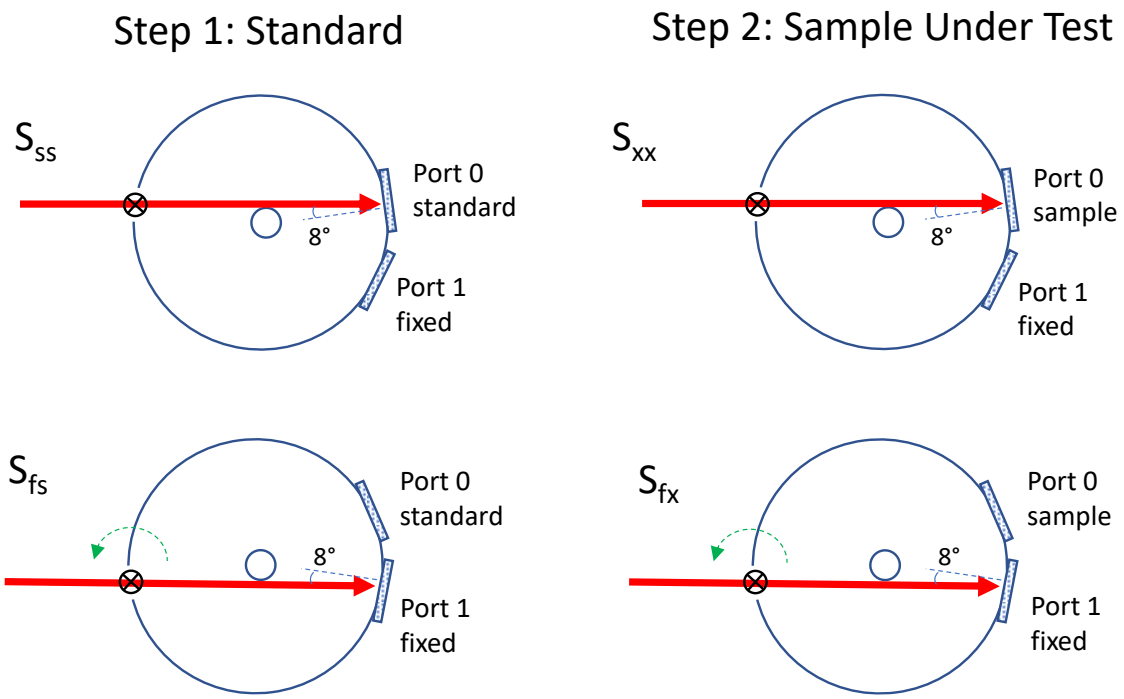

Fig. 8. Substitution mode measurement sequence for the RIS.

4.4. Common Operating Procedures

The supercontinuum source, laser-driven light source, and EIGA detector cooling are turned on at least 30 minutes prior to a calibration. Data are saved in a database and copied to software for further processing. The data are also backed up to controlled directories on NIST's internal servers. A check standard measurement using the appropriate geometry is always performed prior to each calibration. Check standards include mirrors, sintered PTFE samples, and white matte ceramics. Check standard measurements follow the calibration procedures listed above, except that sample thickness and wedge are not remeasured.

5. Data Analysis and Uncertainties

5.1. Reflectance Calculation

5.1.1. Specular Reflectance

For specular measurements, the sample reflectance is the ratio of reflected to incident flux. The sample specular reflectance, ρ, is calculated using

$$\rho = \frac{S_\mathrm{r}}{S_\mathrm{i}}. \tag{1}$$

The signals S_r and S_i are measured using either silicon or EIGA detectors, depending on the wavelength, normalized by the monitor signal. Characterization of the uncertainties in these signals are discussed in Section 5.2.1. The polarization of the incident light is also important. Measurements are made using linearly polarized incident light. The measurements are made using p-polarization, with the electric field polarization in the plane of incidence, and s-polarization, where the electric field polarization is perpendicular to the plane of incidence. The average of the two component results is taken to produce the result for unpolarized light.

5.1.2. Bidirectional Reflectance

The bidirectional reflectance is described by the BRDF, f_r. The BRDF is given by [20]

$$f_\mathrm{r} = \frac{S_\mathrm{r}}{S_\mathrm{i} \cdot \Omega'}, \tag{2}$$

where Ω' is the effective projected solid angle and is given by the solid angle Ω subtended by the detector aperture, multiplied by the surface projection $\cos\theta_\mathrm{r}$ and correction factors which are discussed in Section 5.2.2. While not explicitly called out in Eq. (2), the BRDF of all materials varies with θ_i, ϕ_i, θ_r and ϕ_r, as well as polarization and wavelength of the incident light. For a non-uniform sample, it will also vary with illuminated position. f_r in Eq. (2) has units of inverse steradians (sr^{-1}).

A second quantity often used to describe diffuse reflectance is the directional-directional reflectance factor R, which is the unitless ratio of the BRDF at a given incident and viewing geometry relative to the BRDF of a perfectly reflecting diffuser (PRD) and is given by

$$R = \pi f_\mathrm{r}. \tag{3}$$

The PRD is a theoretical ideal diffuse surface that reflects incident radiation without losses and with a Lambertian directional distribution. The BRDF of a PRD is a constant equal to $1/\pi$, independent of angles, wavelength, and polarization. Hence the reflectance factor shown in Eq. (3) will have values near unity for nearly Lambertian, highly reflecting samples.

5.1.3. Directional-hemispherical reflectance

As described in Section 4.3, the 8/di spectral reflectance factor is determined by comparison to a standard with a known 8/di spectral reflectance factor using a substitution method. The standard is pressed polytetrafluoroethylene (PTFE) [18], and its 8/di reflectance factor is determined using the absolute method of Van den Akker [21]. The 8/di spectral reflectance factor *R* at each wavelength λ is calculated using Eq. (4) below, where S_{xx} and S_{fx} are the average signals with the calibration item on the sphere when illuminating the item and the fixed port, respectively, S_{ss} and S_{fs} are the average signals with the standard on the sphere when illuminating the standard and the fixed port, respectively, and R_{s} is the spectral reflectance factor of the PTFE standard:

$$R(\lambda) = \frac{S_{\mathrm{xx}}(\lambda)}{S_{\mathrm{fx}}(\lambda)} \cdot \frac{S_{\mathrm{fs}}(\lambda)}{S_{\mathrm{ss}}(\lambda)} \cdot R_{\mathrm{s}}(\lambda). \tag{4}$$

Although not explicitly shown in Eq. (4), in practice a set of signals is collected for horizontal and vertical input polarizations and the signal values for both polarizations are averaged to yield the reflectance factor for unpolarized incident radiant flux.

5.2. Uncertainties in bidirectional measurements

5.2.1. Signal

All measurements on the ROSI robotic goniometer are ratios of reflected to incident flux. For example, for specular measurements, the specular reflectance is the ratio of S_{r} to S_{i} so $\rho = S_{\mathrm{r}}/S_{\mathrm{i}}$ (see Eq. 1). The incident and reflected flux at the goniometer receiver are measured using either the silicon or EIGA photodetector, a preamp, and a lock-in amplifier. In addition, a monitor channel, with its own detector, preamp, and lock-in amplifier, is used to compensate for any drift in the light source power. Therefore, in practice ρ is measured as

$$\rho = \frac{S_{\mathrm{r}}}{S_{\mathrm{i}}} = R_{\mathrm{V}} \cdot R_{\mathrm{G}} \cdot R_{\mathrm{L}}, \tag{5}$$

where

$$R_{\mathrm{V}} = \frac{V_{\mathrm{d,r}}}{V_{\mathrm{m,r}}} \cdot \frac{V_{\mathrm{m,i}}}{V_{\mathrm{d,i}}}. \tag{6}$$

The voltage ratio is R_{V}, where $V_{\mathrm{d,r}}$ and $V_{\mathrm{m,r}}$ are the voltages read by the receiver detector and monitor detector lock-ins during the reflected flux measurement, respectively, and $V_{\mathrm{d,i}}$ and $V_{\mathrm{m,i}}$ are the voltages read by the receiver detector and monitor detector lock-ins during the incident flux measurement, respectively. Its uncertainty $u(R_{\mathrm{V}})$, is taken from the root-sum-squared of the relative standard deviation of the mean of 10 consecutive measurements of the four

voltages, multiplied by R_{V}. The additional terms in Eq. (5) are as follows. First, because the gain of the receiver preamp between measurements of incident flux and reflected flux may be changed, especially for BRDF measurements where there are orders of magnitude differences in the reflected and incident signals, we must include R_{G}, the ratio of the receiver pre-amp gain during the incident flux measurement to the receiver pre-amp gain during the reflected flux measurement. Similarly, R_{L} accounts for any difference in the voltage response of the receiver lock-in at the sensitivity settings used during the reflected and incident flux measurements. In practice, the sensitivity of the lock-in is held fixed unless the maximum preamp gain has been reached. It is important to note that because reflectance is a ratio measurement, the absolute gains and sensitivities of the amplifiers and lock-ins need not be known, so long as the relative gains and sensitivities can be obtained. Additionally, because the preamp gain and lock-in sensitivity of the monitor channel are not changed between incident and reflected signal measurements, the gain and sensitivity ratios of the monitor channel do not need to be characterized.

The values and uncertainties of R_{G} and R_{L} for all applicable gain and sensitivity settings of the receiver are characterized by comparing signal levels output by adjacent gain or sensitivity settings for a range of input optical signals generated by a suite of neutral density filters. The filters range from optical density 0.1 to 5.0, allowing characterization of R_{G} and R_{L} for signal ratios $S_{\mathrm{r}}/S_{\mathrm{i}}$ to at least 10^{-5}. To characterize R_{G}, we use combinations of neutral density filters to set several light levels that can be amplified by two adjacent amplifier gain settings without overloading the lock-in when on its fixed, lowest sensitivity. The gain ratio for the adjacent gain settings is the ratio of voltages produced by the two settings. The uncertainty in gain ratio of the adjacent gain settings is taken to be the standard deviation of the gain ratios measured at multiple (typically 4 to 10) light levels. This is done for all adjacent gain settings. Then, because the gain settings between the incident and reflected flux measurements are not always adjacent, we calculate R_{G} for all pairs of gain settings by multiplying all adjacent gain ratios between the two settings. Finally, $u(R_{\mathrm{G}})$ for each pair of gain settings is determined by taking the root-sum-squared of the relative uncertainties of the adjacent gain ratios between the two settings and multiplying by R_{G}. The values of R_{L} and uncertainties $u(R_{\mathrm{L}})$ for the receiver lock-in amplifiers are determined using the same process with the receiver preamp gain held fixed at its highest level. The values of R_{G} can be up to several percent different from the nominal values due to amplifier roll off but are stable so long as the frequency of the optical chopper does not change. The values of R_{L} typically vary by only a few tenths of a percent from the nominal values. The values of the uncertainty components $u(R_{\mathrm{V}})$, $u(R_{\mathrm{G}})$ and $u(R_{\mathrm{L}})$ depend upon the signal levels, detectors, preamp gain levels and lock-in sensitivity levels used in a measurement. The impact of these uncertainties and how they are combined with others is discussed below in Section 5.4.

5.2.2. Solid Angle

For measurements of BRDF, f_r (Eq. 2), and reflectance factor R (recall from Eq. 3 that $R = \pi f_r$), the signal ratio is divided by the effective projected solid angle Ω':

$$\Omega' = \frac{A}{D^2} \cdot C_f \cdot C_e \cdot cos\,\theta_r \quad \textbf{(7)}$$

where *A* is the area of the precision aperture of the ROSI receiver (see Section 3.3), *D* is the distance from the center of the sample face to the precision aperture, and θ_r is the viewing angle. The aperture area *A* was measured and certified by the Aperture Area Facility in the Sensor Science Division at NIST [22]. The distance *D* is measured with the sample holder normal directly facing the receiver and the face of the sample holder at the goniometer center. A cap covers and protects the aperture, and the distance is measured at multiple rotations of the receiver arm, keeping the face of the sample holder pointed directly at the aperture by rotating the robot waist and the receiver arm simultaneously. The distance uncertainty is determined from the standard deviation of the measurements at multiple rotations, combined with the uncertainty in thickness of the aperture cap. The accuracy of the inside micrometer is validated by comparison to a gage block that was measured and certified by the Dimensional Metrology program in the Sensor Science Division at NIST [23]. The nominal values and standard uncertainties for A and D are $A = (1128.636 \pm 0.008)\ \mathrm{mm}^2$ and $D = (657.57 \pm 0.08)\ \mathrm{mm}$. Uncertainty in view angle θ_r is determined using the tunable light source set to 550 nm, a mirror on the sample holder, and a small centering aperture that is mounted on the front of the receiver aperture. The alignment of the light source to the centering aperture was evaluated visually for specular viewing angles θ_r from -80° to +80° and found to have a standard uncertainty of 0.05°. The uncertainties for D and θ_r are sometimes increased if the geometry of the sample adds additional uncertainty. C_f and C_e are near-unity correction factors that account for the effect of the finite size of the illuminated area and precision aperture on solid angle projection, and for differences in collection efficiency for light filling the precision aperture when viewing reflected radiant flux compared to the collection efficiency for the near-collimated incident radiant flux, respectively.

The exact value of C_f depends on the geometry including the incident and viewing angles and is given by [16]

$$C_\mathrm{f} = 1 - \frac{R_\mathrm{a}^2}{D^2} + \frac{R_\mathrm{i}^2}{D^2}\frac{1}{\cos^2\theta_\mathrm{i}}\left[\cos(2\phi)\sin^2\theta_\mathrm{i}\sin^2\theta_\mathrm{r} - \cos(2\theta_\mathrm{r})\frac{3+\cos(2\theta_\mathrm{i})}{4}\right] \quad \textbf{(8)}$$

where R_a is the radius of the receiver precision aperture, R_i is the radius of the incident illumination spot on the sample at normal incidence, *A*, *D,* θ_i, and θ_r are as previously defined, and $\phi = \phi_\mathrm{r} - \phi_\mathrm{i}$ is the difference between the azimuthal angles of incidence and viewing. Eq. (8) assumes that the incident illumination is perfectly uniform over the 10 mm diameter illuminated area. This is not exactly the case due to structure in the light exiting the monochromator aperture. To evaluate the uncertainty in C_f for real, measured incident illumination profiles, a Zernike polynomial expansion was developed for incident illumination [16]. We characterized the incident illumination by collecting a series of profiles using beam profiling cameras over a range from 350 nm to 2400 nm. The C_f using all illumination components from the Zernike polynomial expansion was then calculated for representative

geometries of 0/45 and 0/-45 at each wavelength assuming an isotropic sample. For the 0/45 viewing geometry and an ideal uniform illumination spot, C_f = 0.9992. The values of C_f using the full Zernike expansion varied around the ideal due to beam profile variation with wavelength, and the uncertainty in C_f was taken to be the standard deviation of the values calculated using the Zernike expansion, giving a standard relative uncertainty $u(C_\mathrm{f})/C_\mathrm{f}$ of 0.05%.

The correction factor C_e is needed because the geometric solid angle $A\cos\theta_\mathrm{r}/D^2$ assumes that the efficiency of light collection is the same regardless of whether light is collimated and goes

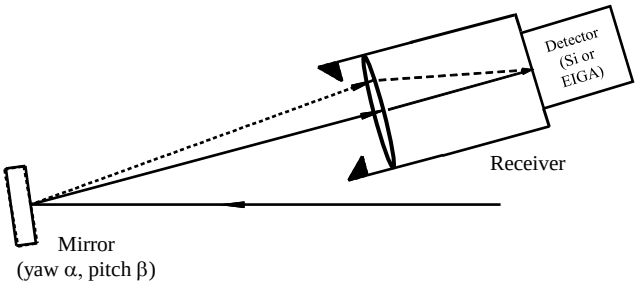

Fig. 9: Setup for scanning underfilling beam over receiver aperture to determine effective solid angle. The receiver is the ROSI receiver described in Section 3.3.

through the center of the aperture or is diffuse and collected over the full aperture. If the optics behind the precision aperture, which include the lens and detector assemblies (for silicon and EIGA detectors) are not uniform in the way they transmit and collect the light, the need for a correction to the solid angle can result. We tested the uniformity of collection and determined C_e using a beam scanning technique. Briefly, a mirror was mounted on the ROSI sample holder and the detector arm was positioned to collect the beam, which underfills the receiver aperture, as shown in Fig. 9. Note the distance from mirror to receiver has been greatly compressed in the figure to illustrate the measurement concept. The beam was scanned in pitch α and yaw β in a grid of uniform steps $\Delta\alpha$ and $\Delta\beta$ of 0.2° over the aperture. It can be shown that the effective solid angle Ω_eff measured by the scanning procedure is given by

$$\Omega_\mathrm{eff} = \frac{4}{S_{00}}\sum_{\alpha,\beta} S_{\alpha\beta}\cos\alpha\cos^2\beta\,\Delta\alpha\Delta\beta, \quad \textbf{(9)}$$

where S_{00} is the signal measured when the beam is passing through the center of the aperture (specular position), $S_{\alpha\beta}$ is the signal when the mirror is at angle pair (α,β), and angles are measured in radians. The beam scan was carried out at multiple wavelengths to get an average and standard deviation of Ω_eff using each of the two detectors of the ROSI receiver: the directly illuminated silicon photodiode for the UV-NIR and the EIGA on a small integrating sphere for the SWIR. For each detector, we then calculated the correction factor C_e from

$$C_{\mathrm{e}} = \frac{\Omega_{\mathrm{eff}}}{\Omega} \tag{10}$$

In the case of the integrating sphere-mounted EIGA detector, the collection efficiency for diffusely scattered light was about 0.6% higher than that for the collimated incident light that was centered on the precision aperture. In the case of the directly illuminated silicon detector, there was negligible difference in the efficiency of diffusely scattered light compared to collimated incident light. Combining the standard deviation of the measurements of Ω_{eff} with the estimated accuracy of the model given the illumination beam size and step size of the scan, we conclude that $C_{\mathrm{e}} = 1.0002$ and $u(C_e) = 0.0032$ for the silicon detector and $C_{\mathrm{e}} = 1.0058$ with $u(C_e) = 0.0021$ for the EIGA detector on the sphere.

5.2.3. Sample-dependent Uncertainty Components

In addition to variables that appear explicitly in Eqs. (1) through (3), the specular reflectance ρ, BRDF f_r, and reflectance factor R for practical samples are always dependent upon quantities that do not appear explicitly in the measurement equation, such as wavelength, polarization, and incident and viewing angles. For example, the BRDF for an in-plane measurement might depend upon incident angle, viewing angle, wavelength, and polarization: $f_{\mathrm{r}}(\theta_{\mathrm{i}}, \theta_{\mathrm{r}}, \lambda, \sigma)$. If the quantities inside the parentheses are labeled as variables q_i, then the uncertainties $u(q_i)$ in these quantities lead to additional relative uncertainty components $u_{\mathrm{rel},f_{\mathrm{r}}}(q_i)$, which are uncertainties in f_{r} due to the q_i, calculated from the derivative of f_{r} with q_i

$$u_{\mathrm{rel},f_{\mathrm{r}}}(q_i) = \frac{1}{f_{\mathrm{r}}}\frac{\partial f_{\mathrm{r}}}{\partial q_i}u(q_i), \tag{11}$$

which are added in quadrature (that is, root-sum-squared) to the other relative uncertainty components to calculate the relative standard uncertainty in f_{r}. Common q_i that give significant uncertainty components are wavelength, with $u(\lambda)$ = 0.7 nm, and incident and viewing angles, with typical $u(\theta_{\mathrm{i}}) = u(\theta_{\mathrm{r}}) = 0.05°$ for ideal samples, but which may be larger for samples with significant wedge angle (see Section 4.2).

Another sample-dependent uncertainty component arises when the value of BRDF, reflectance, or reflectance factor is found to be dependent upon position on the sample. This is expressed as a sample uniformity uncertainty, $u(U_{\mathrm{s}})$ that is evaluated from the standard deviation of the measurand at multiple locations on the sample and leads to a relative uncertainty component

$$u_{\mathrm{rel}}(U_{\mathrm{s}}) = \frac{1}{f_{\mathrm{r}}}u(U_{\mathrm{s}}). \tag{12}$$

While generally insignificant for spectrally neutral samples, an additional sample-dependent component is stray light, that is, light reaching the detector during incident or reflected light measurements that is not at the intended wavelength or that originates from any other unintended source. Further details regarding the evaluation of uncertainty due to stray light are given in [10].

5.2.4. Additional Uncertainty Components

Additional uncertainty components are components that do not affect the value of the measurand, do not appear explicitly in the measurement equation, but nonetheless add uncertainty. These components are modeled as multiplicative factors to the measurement equation with a value of unity, so the standard uncertainty and the relative standard uncertainty are the same. The first such component is receiver/monitor gain ratio stability, $u_{\mathrm{rel}}(R_{\mathrm{S}})$, which accounts for any drift of the relative responsivity and pick-off efficiency between the receiver and monitor detectors between incident and reflected flux measurements. The value of $u_{\mathrm{rel}}(R_{\mathrm{S}})$ was determined to be 0.04 % for the silicon detector and 0.08 % for the EIGA detector from stability measurements made over multiple hours representative of the typical measurement times. Next, detector uniformity contributes to reflectance/scatter uncertainty because different parts of the silicon detector, or different areas of the sphere wall for the EIGA detector, are illuminated during the incident signal and scatter/reflected signal measurements. For specular measurements, the detector uniformity uncertainty $u_{\mathrm{rel}}(U_{\mathrm{D}})$ was found to be 0.04 % for the silicon detector, and 0.01 % for the EIGA detector on the sphere. In the case of diffuse measurements (BRDF or reflectance factor) the detector uniformity uncertainty is included as part of the receiver collection efficiency uncertainty $u(C_{\mathrm{e}})$ discussed in Section 6.2. Finally, an additional component for diffuse measurements, $u_{\mathrm{rel}}(C_{\mathrm{I}})$ (illumination centering), arises from our imperfect ability to center the illumination beam in the goniometer. If the incident beam is shifted laterally at the sample plane towards or away from the receiver, the distance D and viewing angle θ_{r} are altered slightly. The shift in D and θ_{r} are calculated geometrically assuming a standard uncertainty in centering of 0.5 mm and are incident- and viewing-angle dependent. The calculation is detailed in [10] and has a value of 0.16% for the 0/45 geometry.

5.3. Uncertainties in directional-hemispherical measurements

Directional-hemispherical reflectance is calculated from measurements of the detector signals given in Eq. (4) using the procedure described in Section 4.3. Uncertainty components for directional-hemispherical measurements are limited to the uncertainty due to wavelength, which is evaluated from the derivative of the spectral reflectance factor in the same way as described in Section 5.2.3, the uncertainty in the directional-hemispherical spectral reflectance factor of the PTFE standard, and the uncertainty in the signal components of Eq. (4) due to detector noise. In directional-hemispherical measurements, the detector gains and lock-in amplifier sensitivities are not changed between wall and sample measurements, so there are no added signal uncertainties from gain and sensitivity ratios.

The dominant uncertainty component in directional-hemispherical reflectance is typically the uncertainty in the reflectance factor of the pressed PTFE standard. Table 3 lists the relative standard uncertainty currently assigned to the pressed PTFE standard, as a function of wavelength.

Table 3: Uncertainty in 8/di reflectance factor of a pressed PTFE standard, *k* = 1 coverage factor.

Wavelength Range	Relative Standard Uncertainty
250 nm to 350 nm	0.4%
> 350 nm to 400 nm	0.3%
> 400 nm	0.2%

The reference values for reflectance factor of pressed PTFE are given in [19] and were originally assigned a wavelength-independent uncertainty of 0.2%. However, over the years concerns arose that the uncertainties were larger in the UV. In determining the uncertainties in Table 3, we considered differences in UV reflectance seen from multiple sources of PTFE powder and an exploratory comparison of reflectance determined by integrating BRDF measurements of pressed PTFE made on the ROSI goniometer, as a function of wavelength, to the values assigned in [19]. In both cases we found reflectance differences that increased with decreasing wavelength in the UV region. The uncertainties assigned in Table 3 reflect the results of these measurements. The reference values for reflectance factor were not changed. Further investigation of standards and uncertainties for directional-hemispherical measurements is ongoing.

5.4. Example uncertainty calculation and uncertainty budget

Measurement uncertainty is propagated according to the *Guide to the Expression of Uncertainty Measurement* (GUM) [24]. Given a measurement equation of the form $y = f(x_1, x_2 \ldots\ldots)$ the squared combined uncertainty $u_c^2(y)$ is

$$u_c^2(y) = \sum_{i=1}^{N} \left(\frac{\partial f}{\partial x_i}\right)^2 u^2(x_i). \quad \textbf{(13)}$$

In Eq. (13), the $\partial f/\partial x_i$ are referred to as the sensitivity coefficients calculated from the measurement equation and $u(x_i)$ is the uncertainty in each term. Equation (13) assumes that the uncertainties in the input quantities x_i are uncorrelated, which is a reasonable assumption for the uncertainty components described in the previous sections.

For measurement equations where $f(x_1, x_2 \ldots\ldots)$ is a multiplicative function, which is the case for reflectance measurements, it is convenient to describe the combined uncertainty and the component uncertainties as relative uncertainties. The relative combined uncertainty is found using Eq. (13) including the uncertainty components described in the previous sections if they are appropriate to the measurement type. In addition to the uncertainty components from variables that appear explicitly in the measurement equation, we add the uncertainty components described in Section 5.2.3 that do not explicitly appear in the measurement

equation, but for which there is a measurement dependence, for example, wavelength or sample uniformity. As an example, the combined relative uncertainty for a measurement of BRDF in the 0/45 geometry is given by:

$$\frac{u_c^2(f_r)}{{f_r}^2} = \frac{u^2(R_V)}{{R_V}^2} + \frac{u^2(R_G)}{{R_G}^2} + \frac{u^2(R_L)}{{R_L}^2} + \frac{u^2(A)}{A^2} + \frac{4u^2(D)}{D^2} + \frac{u^2(C_f)}{{C_f}^2} + \frac{u^2(C_e)}{{C_e}^2} + \left(\frac{1}{f_r}\frac{\partial f_r}{\partial \theta_r} - \tan\theta_r\right)^2 u^2(\theta_r) + \left(\frac{1}{f_r}\frac{\partial f_r}{\partial \lambda}\right)^2 u^2(\lambda) + \left(\frac{1}{f_r}\frac{\partial f_r}{\partial \theta_i}\right)^2 u^2(\theta_i) + u_{rel}^2(C_I) + u_{rel}^2(R_S) + u_{rel}^2(U_S). \quad (14)$$

Typical relative uncertainty components for the terms in Eq. (14) for the case of a 0/45 BRDF measurement using the silicon detector over visible wavelengths are given in Table 4.

Table 4. Uncertainty Components in the Case of a 0/45 BRDF Measurement

Uncertainty Component	Uncertainty Term	Representative Relative Uncertainty Value
Aperture Distance, *D*	$2u(D)/D$	0.0003
Aperture Area, *A*	$u(A)/A$	< 0.0001
Viewing Angle, $\boldsymbol{\theta_r}$	$\frac{1}{f_r}\frac{\partial f_r}{\partial \theta_r} - \tan\theta_r$	0.0009
Finite Solid Angle Calculation, C_f	$u(C_f)/C_f$	0.0005
Illumination Centering, C_I	$u_{rel}(C_I)$	0.0016
Receiver Efficiency Uniformity, C_e	$u(C_e)/C_e$	0.0032
Detector Gain Ratio, R_G	$u(R_G)/R_G$	0.0006
Lock-in Amplifier Sensitivity Ratio, R_L	$u(R_L)/R_L$	0.0002
Receiver/Monitor Gain Ratio Stability, R_S	$u_{rel}(R_S)$	0.0004
Detector Noise/ Voltage Ratio, R_V	$u(R_V)/R_V$	< 0.0001
Wavelength	$\frac{1}{f_r}\frac{\partial f_r}{\partial \lambda}u(\lambda)$	< 0.0001
Sample Uniformity	$u_{rel}(U_s)$	0.0004

Incident Angle	$\frac{1}{f_r}\frac{\partial f_r}{\partial \theta_i}u(\theta_i)$	< 0.0001
Combined Relative Standard Uncertainty	$u_{\mathrm{c}}(f_{\mathrm{r}})/f_{\mathrm{r}}$	0.0038
Expanded Combined Relative Uncertainty (k = 2)	$U_{\mathrm{rel}}(f_{\mathrm{r}})$	0.0077

Values listed as < 0.0001 are very small and are ignored in the calculation of combined standard uncertainty. The expanded combined relative uncertainty is obtained by multiplying the combined relative standard uncertainty by a coverage factor $k = 2$. To obtain the absolute expanded combined uncertainty in f_{r}, $U(f_{\mathrm{r}})$, the value $U_{\mathrm{rel}}(f_{\mathrm{r}})$ is multiplied by f_{r}. Note that although Eq. (14) and Table 4 are written in terms of BRDF f_{r}, the relative uncertainty components for reflectance factor R are identical.

Table 4 does not represent the uncertainty budget for specular reflectance and directional-hemispherical reflectance, which involve fewer uncertainty components and generally have lower uncertainty. Example uncertainty budgets for specular reflectance and directional-hemispherical reflectance can be found in the sample calibration reports in Appendix A. In the case of a specular measurement, the only uncertainty components considered are those associated with detector gain ratio, receiver/monitor gain ratio stability, detector uniformity, detector noise, wavelength, sample uniformity, and sample alignment. Typical $k = 2$ uncertainty $U(\rho)$ in specular reflectance ρ for highly a reflective, spectrally neutral mirror is 0.001 to 0.002. In the case of a directional-hemispherical measurement, the only uncertainty components considered are those associated with the reference standard, detector noise, and wavelength. Typical $k = 2$ uncertainty $U(R)$ in directional-hemispherical reflectance R for a highly reflective, spectrally neutral diffuse reflector is 0.004 in the VIS-SWIR, with larger uncertainties in the UV as discussed in Section 5.3.

6. Validation and quality control

Calibration measurements on ROSI and the RIS comply with the NIST Quality System [13], which in turn conforms to ISO/IEC Standard 17025 [14]. As part of quality control, proper operation of ROSI and the RIS is validated through periodic measurements of check standards and the maintenance of control charts on these standards. The check standards are meant to be representative of calibrated samples and span the range of operation. Check standards include mirrors, sintered PTFE samples, and white matte ceramics.

ROSI and the RIS have also been validated through comparison measurements of representative samples with the prior national reference instrument, STARR. STARR has been validated in multiple international comparisons and through bilateral comparisons with other National Metrology Institutes [4] [25]. Below, we present comparison measurements on a first-surface aluminum mirror and sintered white PTFE samples.

6.1. Validation of 6/-6 specular reflectance

A first-surface aluminum mirror was measured on ROSI and on STARR. Figure 10 shows this mirror's reflectance for unpolarized light, in the 6/-6 geometry, at select wavelengths between 250 nm and 2250 nm, as measured by the two instruments. Refer to Fig. 1 for the measurement geometry. Figure 11 plots the difference ROSI – STARR (solid circles), along with confidence bounds (solid lines) derived from the combined uncertainty of measurements on the two instruments. The combined uncertainty is the $k = 2$ uncertainty in the measurements of the two instruments added in quadrature and corresponds to an approximate 95% confidence level. As can be seen, the agreement is excellent, and the data in the two figures demonstrate the equivalence of the specular measurements on the two instruments.

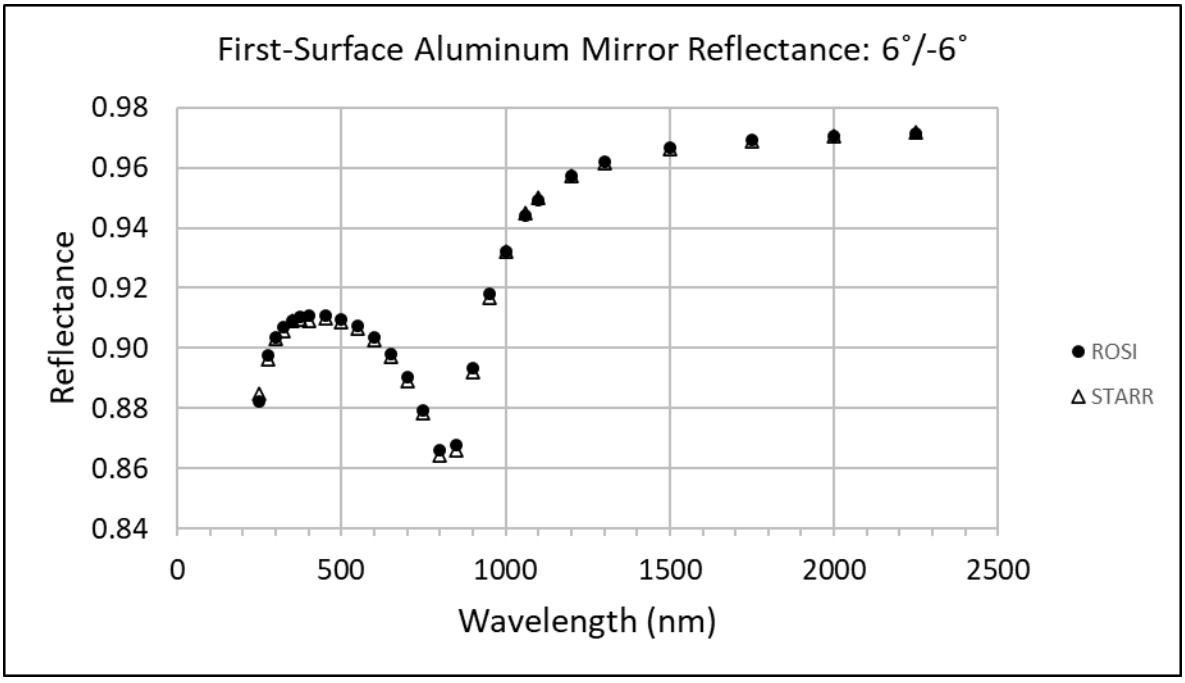

Fig. 10. 6/-6 reflectance of a first-surface aluminum mirror for unpolarized light.

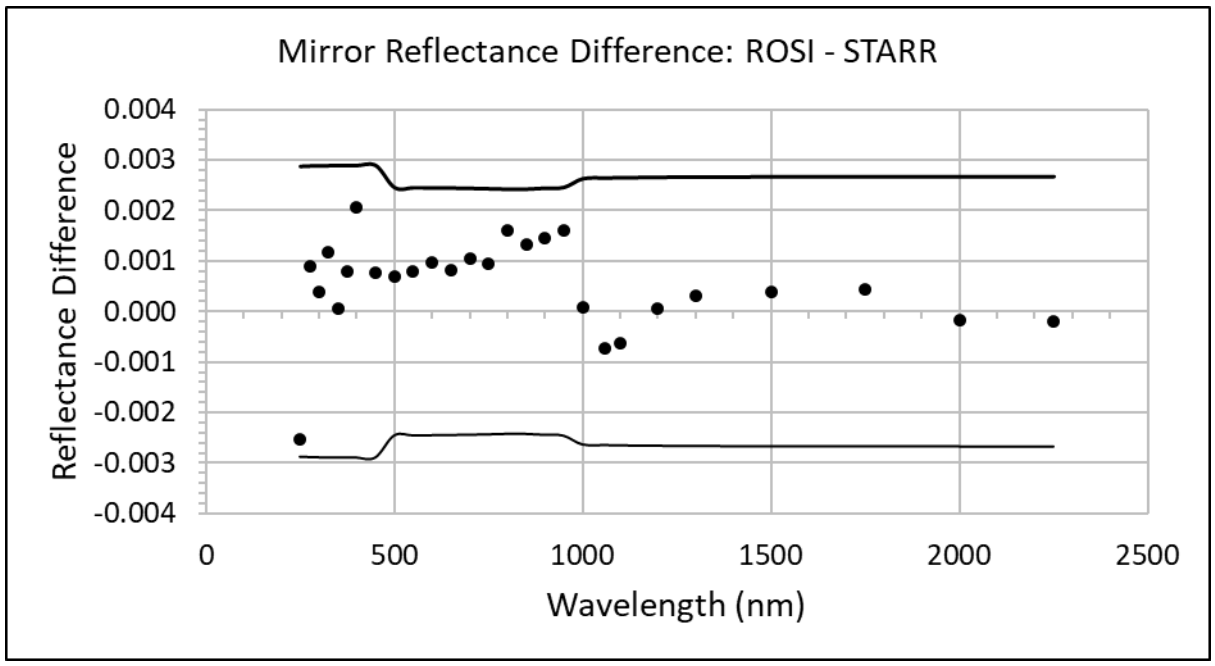

Fig. 11. Difference of the data in Fig. 10, and the *k* = 2 combined uncertainty.

6.2. Validation of 0/45 Reflectance Factor

A white sintered PTFE sample has been measured for its 0/45 reflectance factor in the case of unpolarized incident light using both ROSI and STARR. Figure 12 shows the results for the two instruments. Figure 13 plots the difference ROSI – STARR (solid circles), along with the *k* = 2 combined uncertainty of the two measurements (solid lines), again calculated from adding the *k* = 2 uncertainty in the individual measurements in quadrature. The measurement results have generally been found to lie within the 95% confidence level of the two instruments.

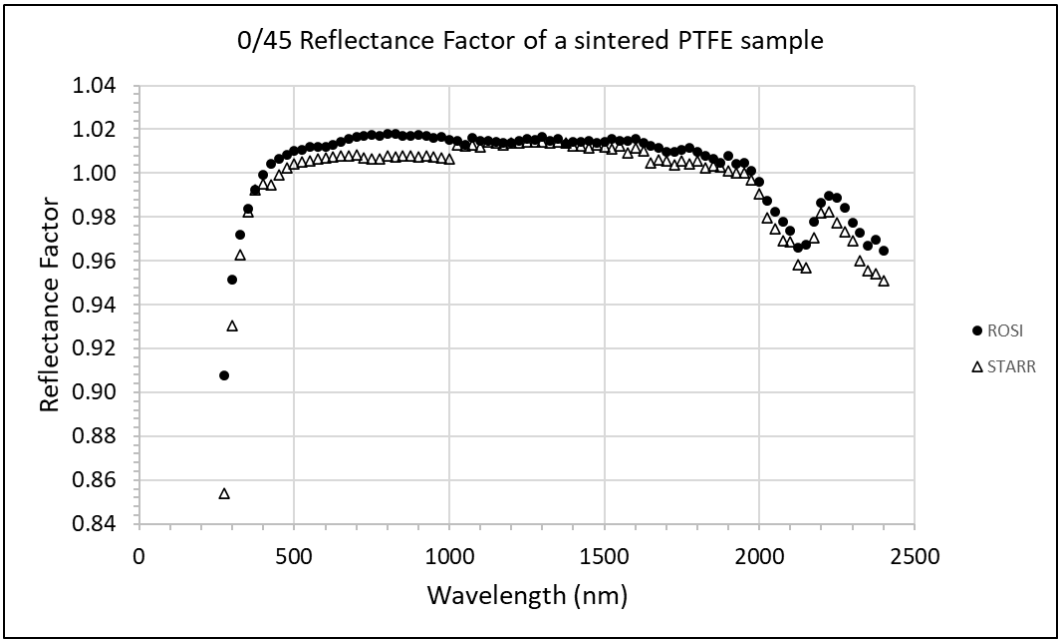

Fig. 12. Reflectance factor of a white sintered PTFE plaque measured by ROSI and STARR.

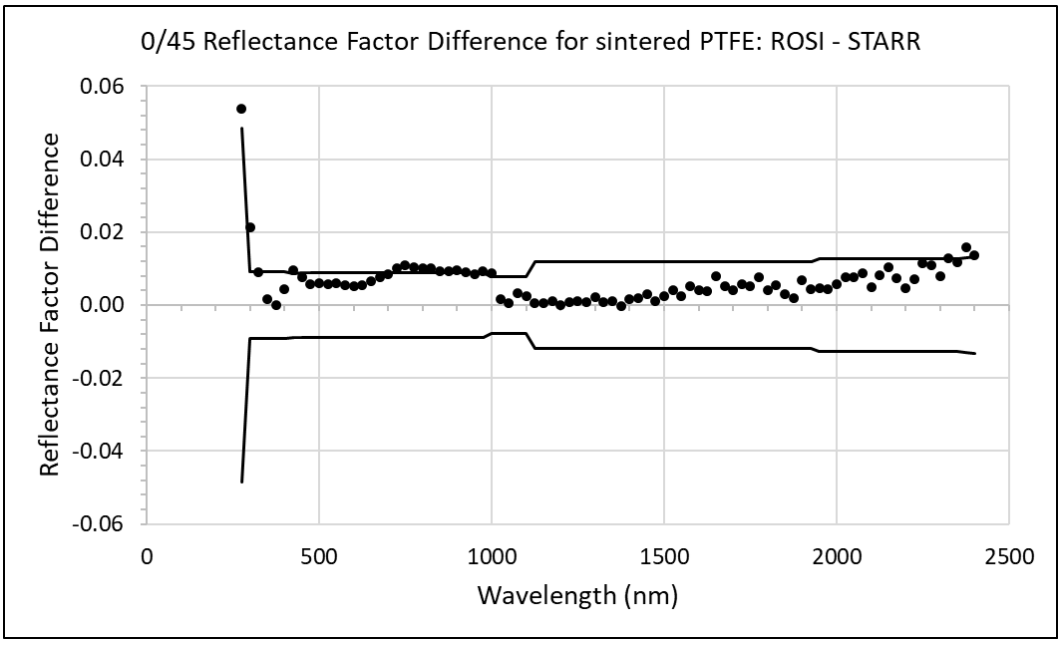

Fig. 13. Difference of the data in Fig. 12, and the combined *k* = 2 uncertainty.

6.3. Validation of directional-hemispherical reflectance

A sintered white PTFE sample was measured for directional-hemispherical reflectance on both RIS and the STARR integrating sphere. Figure 14 shows the results for the two instruments. Figure 15 plots the difference RIS – STARR (solid circles) and the *k* = 2 uncertainty for the STARR measurement as confidence bounds (solid lines). The calculation of confidence bounds on the difference of directional-hemispherical measurements is complicated by the fact that each measurement uses a

pressed PTFE reference standard, leading to correlated components of uncertainty between the two instruments that would be double counted using the root-sum-squared of the uncertainties for both measurements. While the rigorous separation of uncorrelated and correlated uncertainties for the standard, and for past measurements on STARR, is difficult, we can reduce double counting by considering only STARR's uncertainty when establishing the confidence bounds on the difference. The agreement of the difference RIS – STARR is well within the STARR uncertainty, validating RIS for directional-hemispherical reflectance.

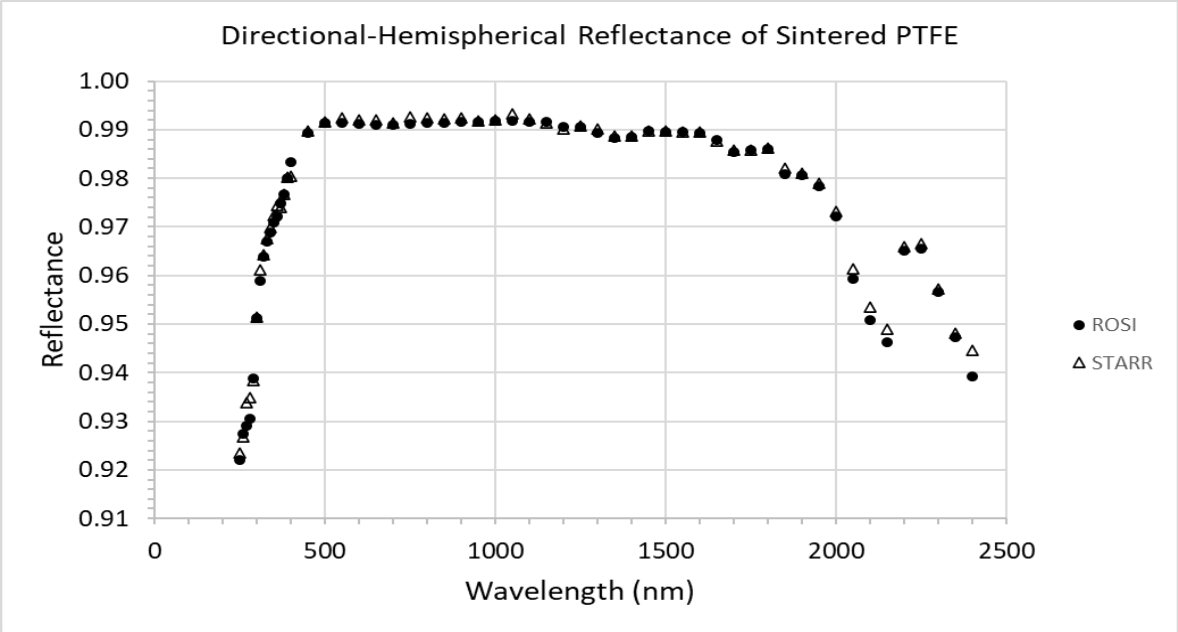

Fig. 14. Directional-hemispherical reflectance of a sintered PTFE sample measured by RIS and STARR.

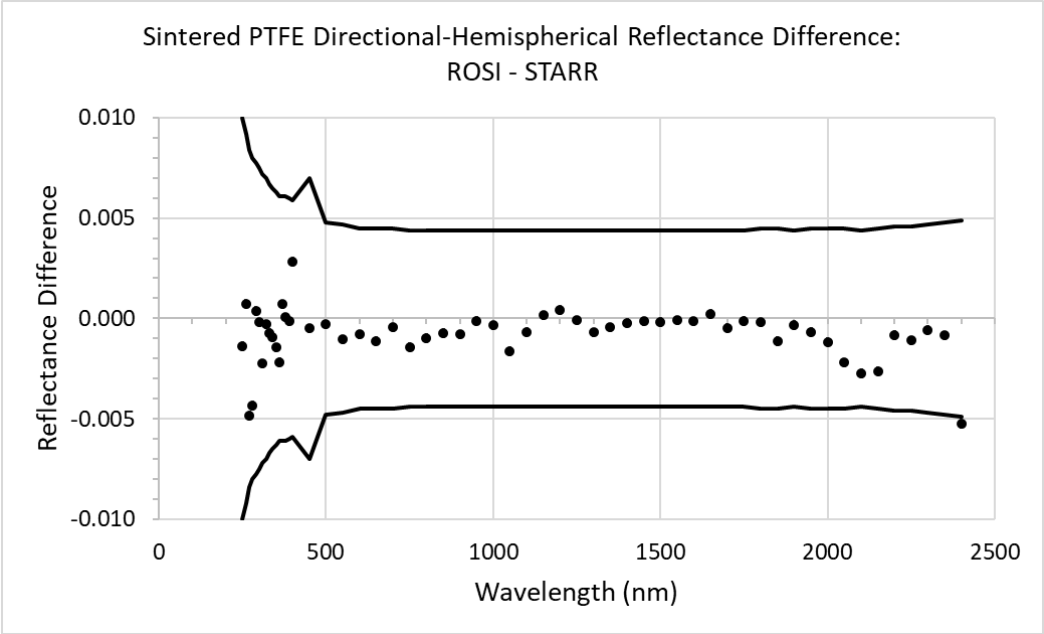

Fig. 15. Difference of the data in Fig. 14, and confidence bounds as described in the text.

References

[1] P. Y. Barnes, E. A. Early, and A. C. Parr, “Spectral Reflectance,” NIST Special Publication 250-48 (NIST, 1998).
[2] F. E. Nicodemus, J. C. Richmond, J. J. Hsia, I. W. Ginsberg and T. Limberis, “Geometrical considerations and nomenclature for reflectance,” NBS Monograph 160 (1977).
[3] C. C. Cooksey, D. W. Allen, B. K. Tsai and H. W. Yoon, “Establishment and application of the 0/45 reflectance factor scale over the shortwave infrared,” Appl. Opt. 54, 3064-3071 (2015).
[4] C. C. Cooksey, M. E. Nadal, D. W. Allen, K.-O. Hauer and A. Höpe, “Bidirectional reflectance scale comparison between NIST and PTB,” Appl. Opt. **54**, 4006-4015 (2015).
[5] G. Obein, R. Bousquet and M. E. Nadal, “New NIST Reference Goniospectrometer,” Proc. SPIE **5880**, 58800T (2005).
[6] D. Huenerhoff, U. Grusemann and A. Hoepe, “New robot-based gonioreflectometer for measuring spectral diffuse reflection,” Metrologia **43**, S11-S16 (2006).
[7] R. Baribeau, W. S. Neil and E. Côté, “Development of a robot-based gonioreflectometer for spectral BRDF measurement,” J. Mod. Optics, **56**, 1497-1503 (2009).
[8] H. J. Patrick, C. J. Zarobila and T. A. Germer, “The NIST Robotic Optical Scatter Instrument (ROSI) and its application to BRDF measurements of diffuse reflectance standards for remote sensing,” Proc. SPIE **8866**, 886615 (2013).
[9] C. D. Mobley, “Estimation of the remote-sensing reflectance from above-surface measurements,” Appl. Opt. **38**, 7442–7455 (1999).
[10] H. J. Patrick, C. C. Cooksey, T. A. Germer, M. E. Nadal, and C. J. Zarobila, “Bidirectional reflectance capabilities of the NIST Robotic Optical Scattering Instrument,” Appl. Opt. **28**, 8774-8786 (2021).
[11] See https://www.nist.gov/laboratories/tools-instruments/reference-integrating-sphere-spectral-reflectance
[12] See https://shop.nist.gov
[13] See https://www.nist.gov/nist-quality-system
[14] International Organization for Standardization (2017) *ISO/IEC 17025:2017 General Requirements for the Competence of Testing and Calibration Laboratories*. (ISO, Geneva, Switzerland).
[15] T. A. Germer, J. C. Stover and Sven Schröder, “Angle-resolved diffuse reflectance and transmittance,” in *Spectrophotometry: Accurate Measurement of Optical Properties of Materials*, T. A. Germer, J. C. Zwinkels and B. K. Tsai, eds. (Academic Press, New York, 2014), Chapter 8, pp. 291-331.
[16] H. J. Patrick, C. J. Zarobila, T. A. Germer, V. A. Ying, C. A. Cooksey and B. K. Tsai, “Tunable supercontinuum fiber laser source for BRDF measurements in the STARR II gonioreflectometer,” Proc. SPIE **8495**, 84950K-1 (2012).
[17] Stanford Research System, “About lock-in amplifiers,” https://www.thinksrs.com/downloads/pdfs/applicationnotes/AboutLIAs.pdf (accessed 9 May 2023).
[18] P. Y. Barnes and J. J. Hsia, “45°/0° Reflectance Factors of Pressed Polytetrafluoroethylene (PTFE) Powder,” NIST Technical Note 1413 (NIST, 1995).

[19] V.R. Weidner and J.J. Hsia, “Reflection Properties of Pressed Polytetrafluoroethylene Powder,” J. Opt. Soc. Am. **71** No.7 (1981).
[20] Thomas A. Germer, Joanne C. Zwinkels, and Benjamin. K. Tsai, “Theoretical Concepts in Spectrophotometric Measurements,” in *Spectrophotometry: Accurate Measurement of Optical Properties of Materials*, T.A. Germer, J. C. Zwinkels, and B. K. Tsai, Eds. (Academic Press, New York, 2014), Chapter 2, pp. 11–66.
[21] W.H. Venable, Jr., J.J. Hsia, and V.R. Weidner, “Establishing a scale of directional-hemispherical reflectance factor I: The Van den Akker Method,” J. Res. of the National Bureau of Standards **82**, No. 1 29-55 (1977).
[22] J.B. Fowler and M. Litorja, “Geometric Area Measurements of Circular Apertures for Radiometry at NIST,” *Metrologia*, **40**, no. 1, S9-S12 (2003).
[23] T. Doiron and J. Beers, J. (1995), The Gage Block Handbook, Monograph (NIST MN), National Institute of Standards and Technology, Gaithersburg, MD, [online], https://tsapps.nist.gov/publication/get_pdf.cfm?pub_id=820735 (Accessed July 24, 2024)
[24] BIPM, IEC, IFCC, ILAC, ISO, IUPAC, IUPAP, and OIMI. Evaluation of Measurement Data – Guide to the Expression of Uncertainty in Measurement. Joint Committee for Guides in Metrology, JCGM 101:2008.
[25] M. Nadal, K.L. Eckerle, E.A. Early, and Y. Ohno, “Final report on the key comparison CCPR-K5: Spectral diffuse reflectance,” Metrologia 50 (1A), 2013.

Appendix A. Example Calibration Reports

Example calibration reports for spectral specular reflectance, 0/45 spectral reflectance factor, and 8/di spectral directional-hemispherical reflectance are available at the links below.

A.1. Specular Spectral Reflectance

https://doi.org/10.6028/NIST.SP.250-101sup1

A.2. 0/45 Spectral Reflectance Factor

https://doi.org/10.6028/NIST.SP.250-101sup2

A.3. Directional-Hemispherical Reflectance Factor

https://doi.org/10.6028/NIST.SP.250-101sup3